nature communications

Article

https://doi.org/10.1038/s41467-024-55670-4

Multidimensional free shape-morphing flexible neuromorphic devices with regulation at arbitrary points

Received: 25 March 2024

Accepted: 20 December 2024

Published online: 17 January 2025

Check for updates

Jiaqi Liu[1,2], Chengpeng Jiang[1,2], Qianbo Yu[1,2], Yao Ni[1,2], Cunjiang Yu[3,4,5,6] & Wentao Xu[1,2]

Biological neural systems seamlessly integrate perception and action, a feat not efficiently replicated in current physically separated designs of neural-imitating electronics. This segregation hinders coordination and functionality within the neuromorphic system. Here, we present a flexible device tailored for neuromorphic computation and muscle actuation. Each individual device component emulates essential synaptic functions for neural computing, while the collective ensemble replicates muscle actuation in response to efferent neuromuscular commands. These properties stem from densely-packed, hydrophilic nanometer-sized channels, and the erection of a high-entropy, intricately silver nanowires to capture and store of hydrated cations. Leveraging the remarkable deformation effect, we demonstrate hazard detection-avoidance robot, and multidimensional integration for arbitrary programmed shapes like 360° panoramic information capture and soft-bodied biological deformations wherein localized responses to stimuli are harmoniously integrated to achieve arbitrary coordinated motion. These results provide a significant avenue for the development of future flexible electronics and bio-inspired systems.

The intricate organisation and functions, e.g. sensation and movement, observed in biological entities currently surpass the capabilities of electronic and machinery devices in various aspects[1–4]. Understanding and harnessing the 1→N differentiation-integration logic inherent in biological functionalities, and drawing inspiration from this, purposefully expanding and integrating of numerous simple, identical subunits result in the formation of a collectively-characterised entity, presents an opportunity to introduce innovative concepts into the design of flexible electronic devices and systems.

A neuromuscular junction (NMJ) is a type of synapse that connects the end of a motor nerve to a skeletal muscle to control its movements. Thousands of NMJs and muscle fibres coordinate and integrate with each other to enable an organism to accomplish a variety of movements and deformations[5]. The intricate control mechanism by using a variety of NMJ combinations could be referential to the development of soft robots with natural motion and environmental adaptability, endowing these robots with awareness of surrounding changes, and intelligently responsive motions.

[1]Institute of Optoelectronic Thin Film Devices and Technology, Key Laboratory of Optoelectronic Thin Film Devices and Technology of Tianjin, College of Electronic Information and Optical Engineering, National Institute for Advanced Materials, Nankai University, Tianjin, China. [2]Shenzhen Research Institute of Nankai University, Shenzhen, China. [3]Department of Electrical and Computer Engineering, University of Illinois, Urbana-Champaign, Urbana, IL, USA. [4]Department of Materials Science and Engineering, University of Illinois, Urbana-Champaign, Urbana, IL, USA. [5]Department of Mechanical Science and Engineering, University of Illinois, Urbana-Champaign, Urbana, IL, USA. [6]Department of Bioengineering, Materials Research Laboratory, Beckman Institute for Advanced Science and Technology, Nick Holonyak Micro and Nanotechnology Laboratory, University of Illinois, Urbana-Champaign, Urbana, IL, USA. e-mail: cunjiang@illinois.edu; wentao@nankai.edu.cn

To date, materials and devices that emulates singular synapse[6–10] and neuromorphic system[4,11–15], and artificial muscles driven by heat[16], electricity[17], light[18], and other means[19,20] have been developed. An artificial neuromuscular system composed of artificial synapses and artificial muscles is attracting tremendous attention (Supplementary Table 1). However, due to differences in materials and device structures, these components have remained physically separated in previous reports. This separation increases system complexity, requires additional manufacturing process and reduced the reliability and efficiency of the system. A single materials and device system is desired that combines and integrates synaptic information processing with effectors, which is conducive to the further development and integration of neuromorphic systems.

Herein, we demonstrate a device that integrates the functions of neural computing and mechanical actuation in the "differentiated" and "integrated" forms, respectively. The working mechanism is realised by well-confined sub-nanoscale channels in membranes of perfluorosulfonic acid ionomer (PFSA) modified by the addition of polyvinyl alcohol (PVA). This unique architecture permits interactions with differently-sized cations at the molecular level. The placement of an interwoven layer of silver nanowires (Ag-NWs) at one terminus of the nanochannels facilitates the capture and storage of hydrated cations to achieve threshold opening, sensitisation, and desensitisation, which are essential characteristics of sensory receptors. The device exhibits exceptional flexibility and demonstrates precise deformation actuation. This property facilitates the emulation of snail stalk eyes, enabling 360° panoramic information capture. Moreover, we have intricately integrated each micro-unit through patterned design, achieving cross-dimensional control of complex deformations while simultaneously performing neural computing functions. By integrating neural sensing and actuation functionalities in a unified manner, the devices enhance the integration level and functionality of soft electronics, thereby unveiling promising application prospects in domains such as edge intelligence devices, neuromorphic soft robots, and bioinspired electronic systems.

Results

Concept and material characteristics of synapse - motor coupler device

In a vertebrate NMJ (Fig. 1a), the axonal ends of motor neurons lose their myelin sheath and expand to form enlarged ends that are located in the grooves of muscle fibres. The postsynaptic membrane has many folds. Synaptic vesicles release intracapsular Ach into the synaptic cleft when the action potential is transferred to the enlarged terminal of the motor neuron. Ach binds to nicotinic receptors in the muscle membrane activates the motor endplate potential, and thereby causes contraction of the muscle.

In pursuit of replicating the intricate dynamics of NMJ, a synapse-motor coupler device (SMCD) was designed and fabricated (Fig. 1b). The preparation process is illustrated (Supplementary Fig. 1). This structure adopts the concept of unit-cell, integrates the functionalities of neural computation and three-dimensional arbitrary surface flexibility in a single device. The artificial muscle is electrically driven by ionic actuators. Ag-NWs forest was prepared by electrochemical deposition (Supplementary Fig. 2). The working electrode used a porous alumina template (pore diameter 80 nm) that was coated with a gold (Au) layer on one side (Supplementary Fig. 3a, b). Upon applying voltage, Ag^+ ions from the solution infiltrated the pores and were reduced to Ag metal under the influence of the external electric field, and Ag- NWs formed within the pores (Supplementary Fig. 3c). Washing with an alkaline solution exposed the Ag-NW forest, which collapsed to form a chaotic interlaced structure (Supplementary Fig. 4) that provides abundant sites for adsorption and capture of H^+ ions and other hydrated cations. The Ag-NWs forests were then embedded into PVA-modified PFSA ionic polymer to form the functional layer of the SMCD. PFSA consists of a hydrophobic tetrafluoroethylene (TFE) skeleton and a hydrophilic sulfonic acid side chain. The hydroxyl group of PVA can act as a hydrogen donor[19] to form a hydrogen bond with the sulfonic group of PFSA (Supplementary Fig. 3d). The Fourier transform infrared (FTIR) spectrum of PVA-PFSA had a hydrogen bonding single vibration band at 3200 cm^{-1}, which the FTIR spectrum of pure PFSA lacked[21] (Supplementary Fig. 3e). The photos of PVA-PFSA membrance are shown in Supplementary Fig. 3f.

The entire lower surface of PVA-PFSA and half of the upper surface were plated electroless with a sheet of Ag electrodes (Fig. 1b) to model the Schwann cells. To simulate the presynaptic membrane, spot-like Au electrodes were deposited by evaporation over the rest of the upper surface. To visualise the internal architecture of the SMCD, it cut into crosse-section was dissected and observed by element-distribution (EDS) mapping (Supplementary Fig. 3g). The distributions of fluorine (F), sulphur (S), and oxygen (O) were uniform throughout the SMCD; they are mainly contributed by PFSA. Ag was observed in two distinct areas: the Ag-NW forest affixed to Au, and the Ag electrodes. The water migration coefficient[22] of hydrated Na^+ in PFSA is higher than that of H_3O^+, so an ion-exchange step during the device's preparation (Supplementary Fig. 5 and Supplementary Note 5) introduces hydrated Na^+ ions into the SMCD to mimic the effects of Ach in organisms. Because of the Vehicular effects[23,24], hydrated cations can migrate rapidly in these nanometre-sized channels and are partially absorbed and captured by the Ag-NW forest. This mechanism is the reason that the device can simulate synaptic behaviour and muscle movement, which will be discussed in detail in later parts. SMCDs can potentially work as edge-intelligent devices, performing distributed preliminary information pre-processing near the sensing and actuation ends. Compared to centralised information processing, edge-intelligent devices could shorten the distances between sensing, computing and actuating units[25].

Synaptic plasticity regulation of SMCD

The regulation of synaptic weight is the biological basis of information processing in the nervous system. Action potentials result in post-synaptic excitation and excitatory postsynaptic current (EPSC), which increases sharply in a short time[6,26]. SMCD mimics this process when the spot-like Au electrode is stimulated by a spike of − 2 V (Supplementary Fig. 6). When two identical spikes were applied sequentially, the EPSC was significantly higher after the second pulse than after the first (Fig. 2a); this phenomenon emulates paired-pulse facilitation (PPF), which is a typical short-term synaptic behaviour[27].

The reason for the PPF in SMCD is that the short-term spikes can drive hydrated cations in PFSA to the cathode along the nanochannel and then accumulate in the Ag-NW forest capture layer, where they induce the formation of an electric double layer, which rapidly increases the conductivity of the device along the thickness direction. After one spike, the initial accumulation of ions dissipates back to its initial distribution. If a second spike is applied before this dissipation is complete, then the second accumulation of captured hydrated cations sums to the remainder of the first one. PPF can be quantified using, $PPF\ Index = (A_2/A_1) \times 100\%$[28].When the time interval (Δt) between two consecutive presynaptic spikes was 50 ms, the PPF Index of SMCD was 138%. The PPF Index attenuated exponentially to 100% as Δt increased (Fig. 2b). This trend indicates that if Δt is too long, the second pulse cannot effectively amplify the excitatory response.

EPSC and PPF are two typical forms of short-term synaptic plasticity. They significantly affect the nervous system's processing of temporal information, in tasks that include motor control and signal recognition[22]. Using this short-term plasticity, SMCD can accurately recognise the international Morse code and convert it into different EPSC signals (Fig. 2c). The voltage spikes with different spatio-temporal spikes pulses, and widths of 115 ms and 35 ms represent 'dah, -' and 'dit, ·' in Morse code respectively. The corresponding

https://doi.org/10.1038/s41467-024-55670-4

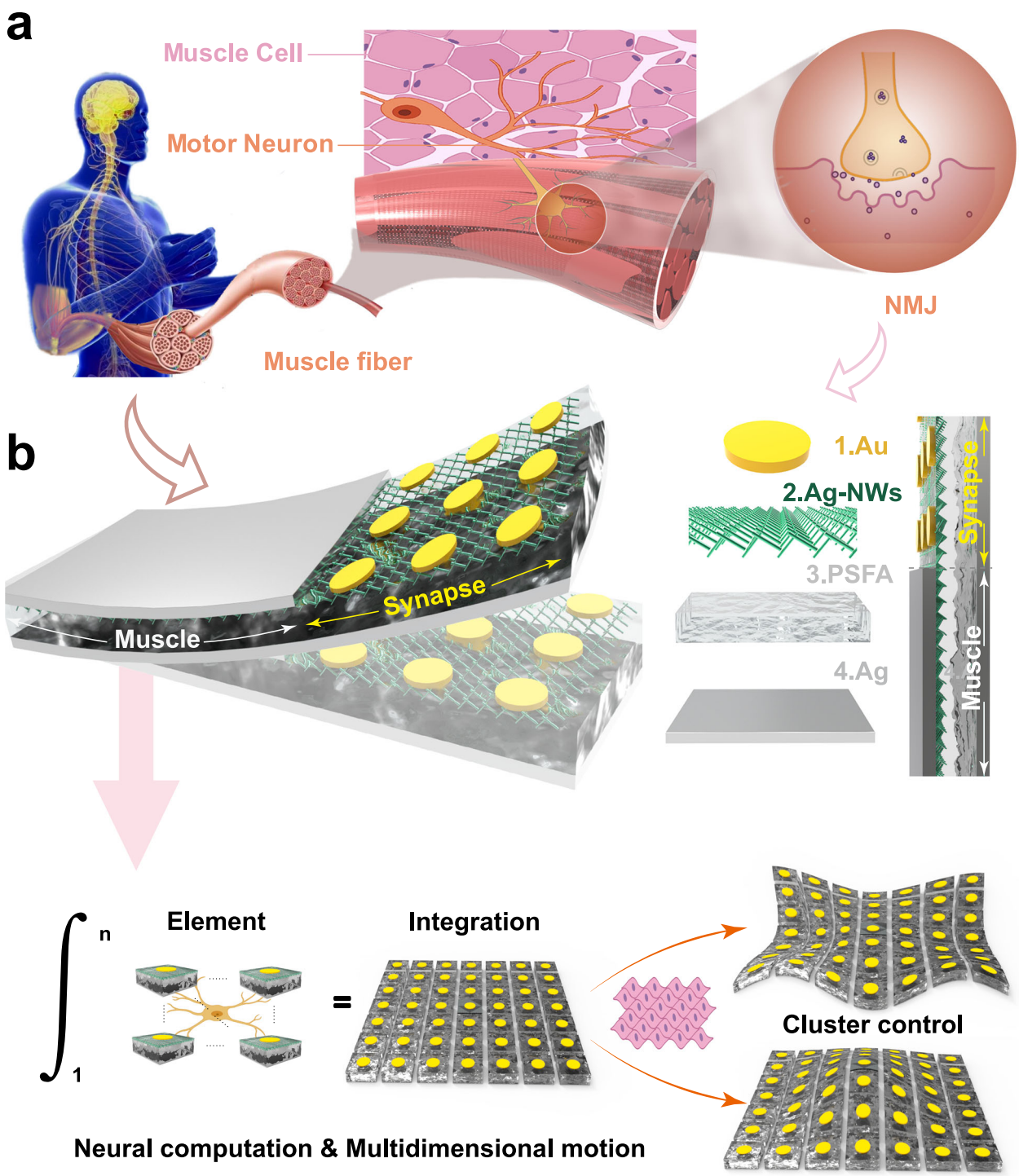

Fig. 1 | Conceptualisation and device structure. a Schematic diagram of the biological neuromuscular interface. **b** Schematic diagram of biomimetic neuromuscular junction named synapse - motor coupler device (SMCD), it consists of four parts: Au, Ag nanowires (Ag-NWs), perfluorosulfonic acid ionomer (PFSA) and Ag.

conversion results of the four letters 'NFEL' are given here (Fig. 2d–g). In this way, the matching between SMCD and wireless communication is realized, which provides a communication method for neuromorphic human-computer interface interaction.

Spike duration (D_S) had a significant effect on the synaptic weight of SMCD. An increase in D_S increases the interval during which hydrated cations are driven into the nanopore channel of PFSA, then migrate to the Ag-NW forest and be captured; therefore, synaptic weight increased as D_S increased (Fig. 2h). The maximum EPSC reached 640 nA. However, the increased D_S begins to saturate the capture sites and decelerates EPSC increase (Supplementary Fig. 7a). This phenomenon is consistent with spike-duration-dependent plasticity (SDDP) in organisms. Increasing the number (N_S) of spikes, increased the number of hydrated cations that migrate to the side of Ag-NW. Spike-number-dependent plasticity (SNDP) was realized on SMCD (Fig. 2i). As the number of voltage spikes increases, more hydrated cations migrate, enhancing the internal electric field and thereby promoting reverse ion migration, which leads to increased EPSC (Supplementary Fig. 8a). Given that the total number of hydrated cations is finite, this process has a maximum spikes

https://doi.org/10.1038/s41467-024-55670-4

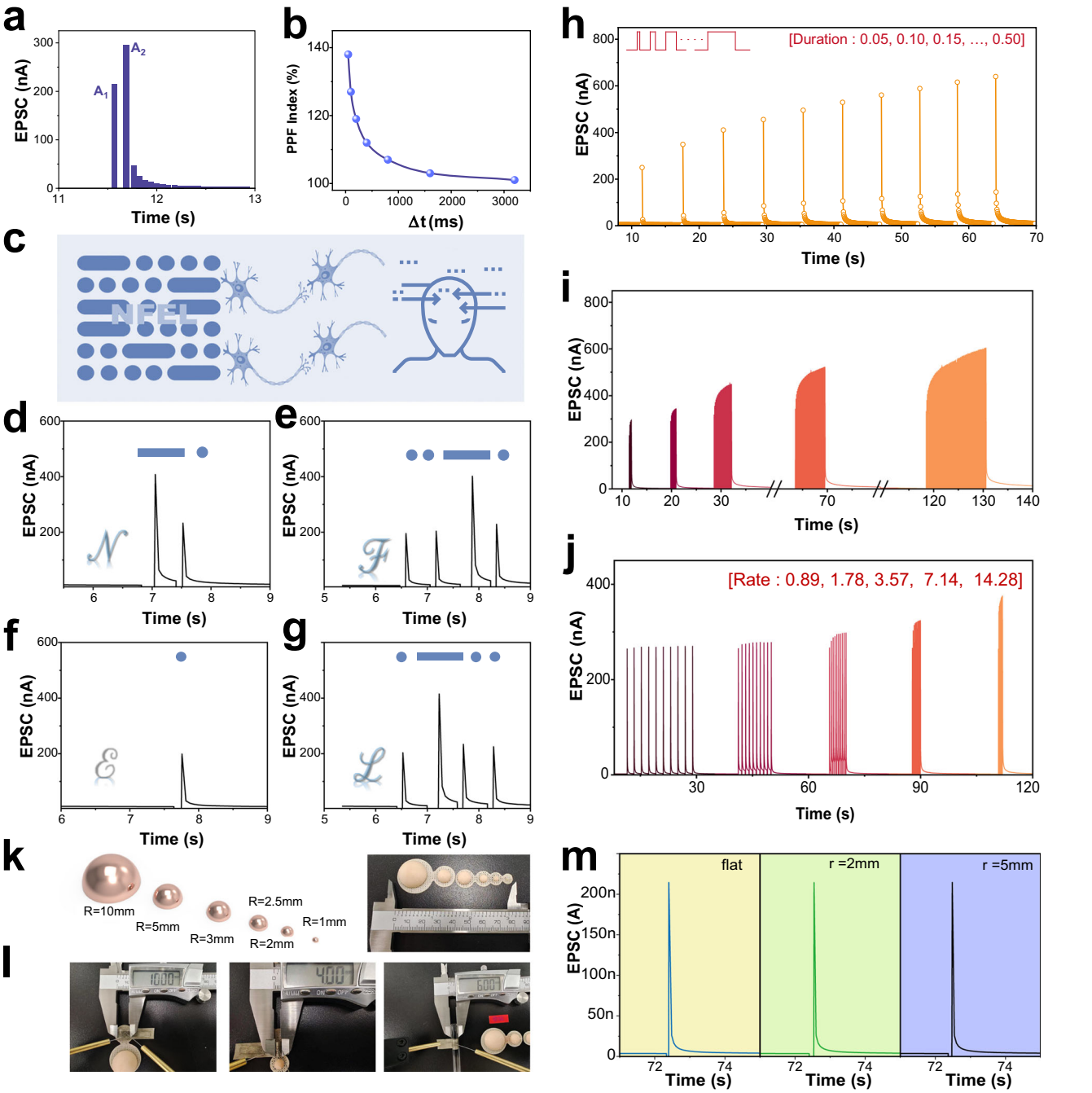

Fig. 2 | Synaptic plasticity simulation and bending testing. a Excitatory post-synaptic current (EPSC) triggered by two consecutive spikes (− 2 V, 60 ms, time interval $\Delta t = 50$ ms). **b** Paired-pulse facilitation (PPF) index as a function of Δt. **c** Short-term plasticity used for Morse code signal recognition schematic diagram and recognition results, (**d**), letter N, (**e**) letter F, (**f**) letter E, (**g**) letter L. **h** Spike-duration-dependent plasticity behaviour of SMCD under different spikes duration widths from 0.035 s to 0.35 s. **i** Spike-number-dependent plasticity of SMCD under 5 ~ 100 consecutive identical spikes (− 2 V, 60 ms), (**j**) Spike-rate-dependent plasticity of SMCD from 0.89 s/spike to 14.28 s/spike. **k** Bending moulds with radii from 10 to 1 mm. **l** Optical images of SMCD during bending tests on the moulds. **m** EPSC response of SMCD under bending to different radii.

accumulation saturation capacity. It was observed that when the number of spikes reached 509, the EPSC growth rate plateaued (Supplementary Fig. 8b, c). Beyond this point, no further EPSC increase occurred.

Increasing the frequency (f_S) of spikes also increased the number of hydrated cations that migrate to the side of Ag-NW. This phenomenon is called spike-rate-dependent plasticity (SRDP), and it is one of the most important forms of synaptic plasticity in biology[25]. When ten consecutive spikes were applied to the SMCD, it showed SRDP (Fig. 2j). At $f_S > 3.57$ spike/s, EPSC gradually increased, f_S increased, and the highest SRDP was 142.64% (Supplementary Fig. 7b). This phenomenon can be exploited for dynamic high-pass filtering. The device is flexible enough to adhere to thermoplastic polyurethanes or glass moulds with different radii. Hemispherical bending moulds of varying sizes were fabricated using 3D printing (Fig. 2k). Subsequently, SMCDs were placed on their tops for testing under different curvatures. Even with a bending radius as small as 2 mm, the EPSC response of the SMCD remained stable (Fig. 2m).

https://doi.org/10.1038/s41467-024-55670-4

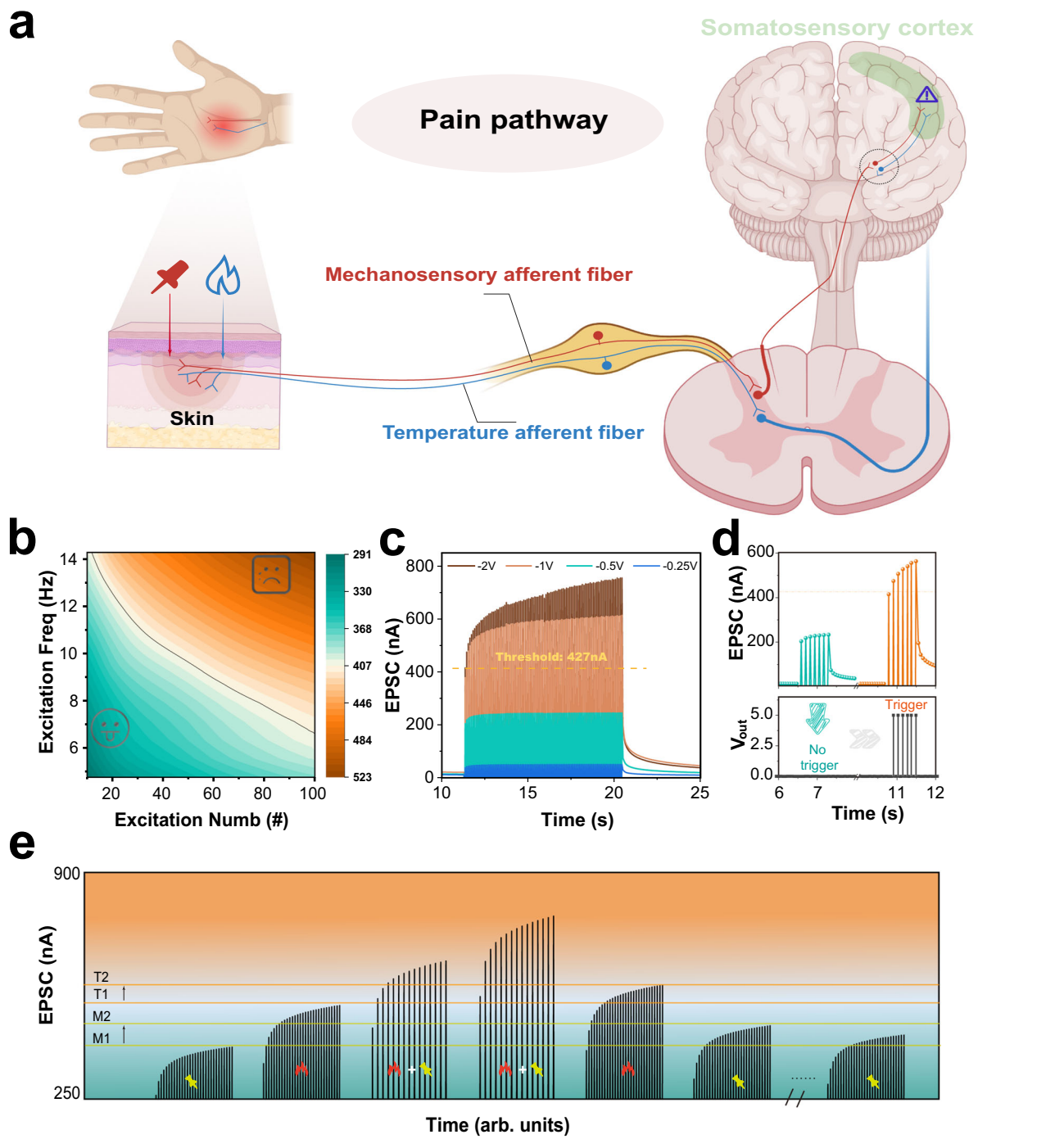

Fig. 3 | Nociceptor simulation of SMCD. a Schematic diagram of human pain perception: orange circle, multi-modal pain sensor, which contains thermal and mechanical dual-mode perception channels. **b** Synaptic weight contour maps at different spikes frequencies and numbers, used to evaluate pain thresholds. **c** EPSC and its relaxation process under 100 consecutive voltage spikes with amplitudes of − 0.25 − 0.5, − 1, or − 2 V. **d** Neuronal threshold triggering effect based on SMCD. **e** Results of bimodal nociceptive stimulus sensitisation. Some elements in Fig. 3a were created in BioRender. Liu, J. (2025) https://BioRender.com/m63a509.

SMCD mimics advanced synaptic behaviour: nociception

Pain is defined as a series of unpleasant sensations caused by real or perceived tissue damage (Fig. 3a)[29]. When nerve endings receive external damage, they generate impulses that pass along an axon to nociceptors, which generate excitatory signals that are integrated and sent to the central nervous system. Simulation of biological pain perception is of great significance to the development of neuromorphic robots[30]. The SMCD shows SRDP and SNDP, so it may be suited to simulate neuron function, such as nociception.

The three main characteristics of nociceptors are threshold, relaxation and sensitisation[31], which can be implemented by SMCD. The result of combined SRDP and SNDP stimulator facilitation mimics a process in which nociceptors are gradually activated under spikes that have the same amplitude (Fig. 3b). An activation threshold current of 427 nA was determined by calculating the 60% weight of the fitted EPSC fitted surface as a function of spikes frequency and quantity (Supplementary Fig. 9 and Supplementary Note 2). This threshold is defined in the manuscript as the sufficient current to activate pain

receptors. Pain signals are produced when signals have that have current above or to the right of the threshold line, whereas typical painless behaviour is shown otherwise. Low frequency of external injury spikes and a small number of them do not cause a response by the SMCD. However, when either the frequency or number of injuries is large enough, the SMCD produces a pain signal; i.e., responds like a nociceptor. The amplitude of the spike also affects the activation of nociceptors. When continuous pulses were applied to the SMCD, EPSC increased as spike amplitude increased (Fig. 3c). When the amplitude of the negative voltage spike exceeded 1 V, the EPSC exceeded a threshold level. After experiencing a harmful irritation, nociceptor undergoes a process of relaxation and recovery. An increase in the amplitude of the spike caused an increase in the time taken for EPSC relaxation to the unexcited statevalue. The phenomenon is similar to the increases in nociceptor arousal and recovery time with an increase in the intensity of a harmful irritation. In addition, we have constructed a threshold-triggering circuit (Supplementary Fig. 10 and Supplementary Note 3) that generates voltage pulses with 110 ms width once EPSC current reaches the threshold, replicating the discharge behaviour of nociceptive neurons (Fig.3d).

Harmful skin irritations include chemical, thermal (hot and cold), and mechanical stimuli. The most common nociceptor in the skin is the multimodal nociceptor (Fig. 3a), which can integrate inputs from sensory receptors that react individually to various stimuli[32]. Thirty consecutive spikes of − 1.2 V were used to simulate mechanical (M) stimulation, and then 30 spikes of − 0.8 V were applied to simulate (non-concurrent) thermal (T) stimulation. After the first stimulation, the maximum EPSC levels reached 517 nA (Fig. 3e, "T1") and 397 nA (Fig. 3e, "M1"). Then, when two probes were used to apply 30 spikes of $M = -1.2$ V and $T = -0.8$ V to SMCD synchronously, the M and T channels were activated at the same time, and the EPSC increased. This increase was repeated when another 30 paired T and M spikes were applied. The behaviour of the SMCD as a nociceptor became evident when it was stimulated by the same sequence of 30 'T' pulses of − 1.2 V pulses, then 30 'M' pulses of − 0.08 V that were applied. In this case, the EPSC was greatly increased to 576 nA (Fig. 3e, "T2") and 459 nA (Fig. 3e, "M2"). This result suggests that multiple injuries sustained over a short period of time sensitise SMCD and, as a consequence, increase the response of the body to the same injury. Through the above demonstration, the three main features of nociceptors have been all successfully simulated by SMCD. These results have demonstrated that the SMCD are capable of threshold opening, sensitisation, and desensitization, which are the three main features of nociceptors.

Motor function and biomimetic design of soft robots based on SMCD

SMCD can not only perform advanced neurological functions but produce a muscle actuation effect (Fig. 4a). When a voltage of − 3 V with a width of 160 ms and a duty cycle of 50% is applied to the Au electrode, the SMCD generates subtle tremor movements, with its current rapidly decreasing after the voltage is removed. In contrast, when exposed to an identical voltage stimulus applied to the Ag electrode, the current signal rapidly saturates, then gradually decreases (Fig. 4b). During these processes, the SMCD bends strongly, by even as much as 360° to form a circle. The mechanism involves the migration of hydrated cations in the applied electrical field. When the voltage is not applied, the hydrated cations in the SMCD are evenly distributed throughout the PFSA. When the voltage is applied, the continuous Ag electrode can form a plate electric field to control a large area of ion migration in SMCD, to increase the proportion of hydrated cations that migrate to the cathode side (Fig. 4a). These hydrated cations migrate rapidly, and when they accumulate, steric interactions among them cause swelling of the cathode side of PFSA-PVA membrane[33], resulting in bending toward the anode side to achieve excitation. One end of the artificial muscle was fixed to create a cantilever beam model, while the free end was precisely aligned with a digital force gauge (Supplementary Fig. 11a). A constant voltage bias of 3 V was applied to the fixed end. After 0.1 sec, a response of 1.3 mN was observed; after 0.85 sec, the output force reached a maximum value of 31.8 mN (Supplementary Fig. 11b, c). Upon application of AC stimulation voltages at varying frequencies, the SMCD deformed cyclically at the same frequencies, showing no obvious time delay (Fig. 4c).

To exploit this deformation effect, we designed an application for the 360-degree panoramic view, mimicking the stalk eyes of a snail (Fig. 4d–g). A stalk-eye of a snail mimic actuator was prepared (Supplementary Fig. 12a). Applying a -3V voltage to the silver electrode induced its rotation, while a lower stimulus voltage served as positional encoding information (Supplementary Fig. 12b). Stimulation of the Au electrode generated EPSC. The trajectory of positional coordinate changes at its endpoints is recorded (Supplementary Fig. 13). The relationship between EPSC variations and positional angles is depicted in Fig. 4e. Figure 4g presents optical photographs of the SMCD positions in the process of movement. To realise the light sensing capability of the stalk eye, we designed a precise electrical connector terminal and used it to integrate a miniature photoresistor, with only 2 mm in size, onto the SMCD (Supplementary Fig. 14a–hand Supplementary Note 4.). We also constructed an angle-dependent gradient light environment (Supplementary Fig. 14j, k and Supplementary Note 4.).The biomimetic stalk eye system was able to accurately discern light intensity differences at various positions around the circle (Fig. 4f), and the SMCD stalk could rotate independently from the body orientation (Supplementary Fig. 15). This demonstrates the system's capability for 360° visual information acquisition, showcasing its intriguing potential in various applications, such as robotics and new energy vehicles, where it can enhance situational awareness and provide a thorough perception of the surrounding environment.

We also fabricated a four-claw Venus flytrap-inspired soft robotics was prepared through laser cutting. By applying a uniform voltage across the entire surface, the closure of soft structures can be effortlessly achieved (Fig. 4h and Supplementary Movie 1). To integrate sensing, neural processing and actuation functions, we designed a close-loop demonstration experiment to showcase the capability of the coupled device to detect and avoid potential obstacles or hazards. We fabricated an SMCD with patterned electrodes (Supplementary Fig. 16 and Fig. 4i). The SMCD was mounted on a crawler-type slider on a sliding rail, with an aluminium plate connected with voltage to simulate a hazardous environment (Fig. 4j). In a safe environment, the robot maintains a forward-thrust posture. Upon encountering the aluminium plate, the robot detects the hazardness and generates EPSC. When the harm threshold is reached (EPSCå 427 nA), stimulation voltage is caused on the muscle drive electrodes, causing the robot to tilt by ~ 60°, thereby breaking contact and escaping from the danger (Fig.4j and Supplementary Movie 2).

Simultaneously, we discovered that by designing and combining the shapes of the electrodes that receive stimulus voltages, we could achieve SMCDs that underwent localised swelling, so arbitrary multi-dimensional deformation could be achieved (Fig. 4k). Specifically, triangular (T), circular (C), and rectangular (L) sub-electrodes were designed on the upper surface of the starfish-shaped soft robot based on SMCD and numbered counter-clockwise as T1-4, L1-4, and C1. Depending on the target state, specific combinations of these sub-electrodes were selected, and applied the voltage (Fig. 4k). This drove the migration of hydrated cations under each selected sub-electrode, causing cathodic swelling and localised deformation in those regions. Consequently, this enabled the soft robot to achieve a series of movement configurations. This mirrors the movement patterns observed in marine invertebrates like starfish, where localised responses to stimuli are integrated to achieve coordinated motion. Prospectively, when facing larger-scale integration designs and higher precision deformation requirements, it will be necessary to integrate

https://doi.org/10.1038/s41467-024-55670-4

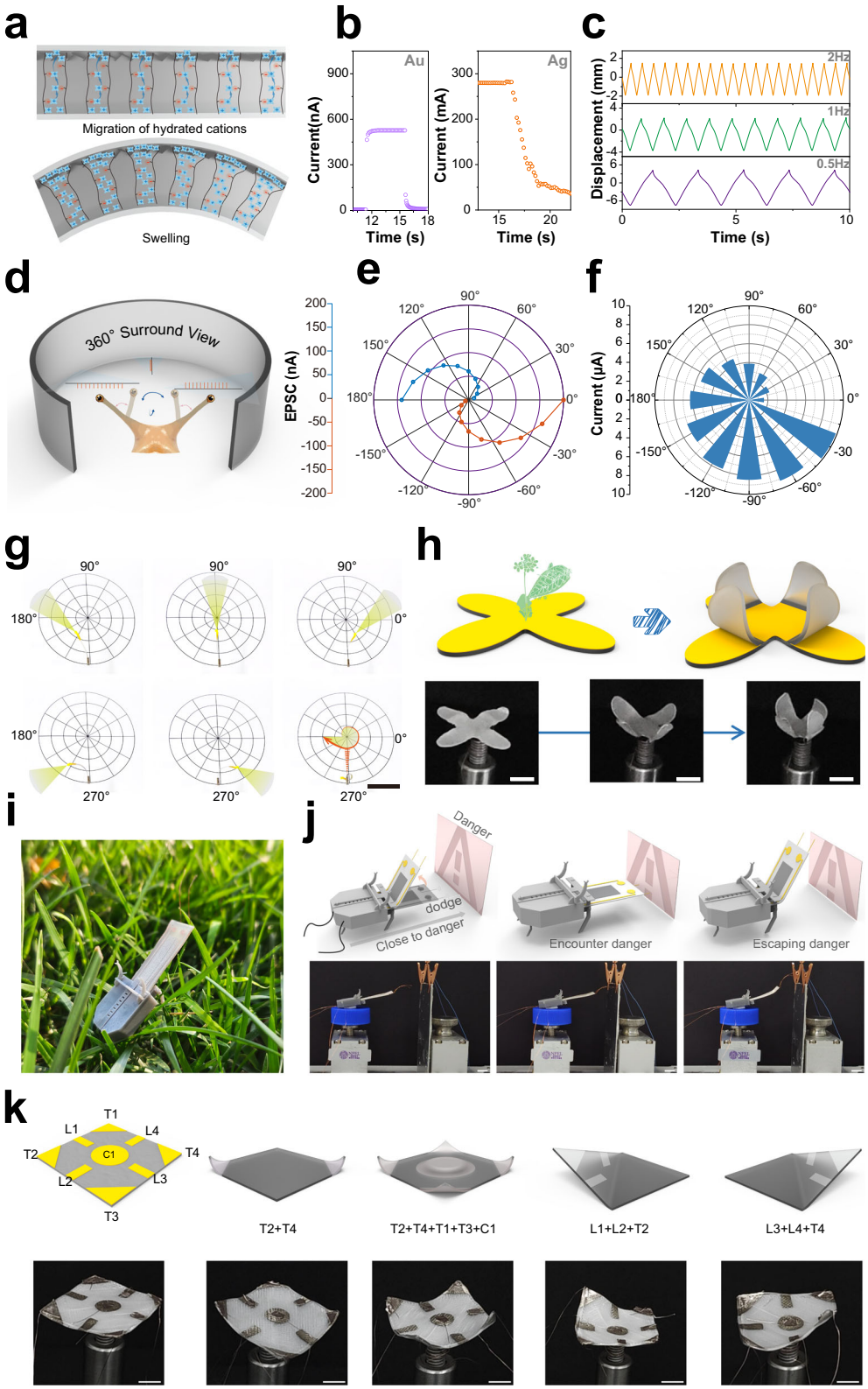

Fig. 4 | Muscle actuation characteristics and biomimetic design of soft robotsbased on SMCD. a Mechanism of SMCD actuation. **b** Current response to a pulse of − 3 V applied to the Au and Ag electrodes. **c** Deformation-displacement statistics of the SMCD under alternating current voltage drive with amplitudes of 3 V and frequencies of 0.5 Hz, 1 Hz, and 2 Hz. **d** Schematic representation of a 360° panoramic view inspired by the stalk eyes of a snail. **e** EPSCs at different angles. **f** Photocurrent statistics of the bionic stalk eye at different angles. **g** Optical photographs of the SMCD during the 360° panoramic viewing process, scale bar: 4 cm. **h** Schematic diagram of Venus flytrap-inspired soft robotics design and optical photographs of the deformation process, scale bar: 1 cm. **i** Digital photograph of a soft robot capable of hazard perception and avoidance based on SMCD. **j** Images and schematic of the robot performing hazard detection and avoidance process, scale bar: 1 cm. **k** Voltage settings for shape programming and correlated photographs of SMCD, scale bar: 1 cm.

advanced integrated circuit manufacturing technologies and asymmetric structure to address issues related to processing and crosstalk[34–36]. Furthermore, a wireless communication module has been further integrated, demonstrating its remote control capabilities in complex task environments, such as underwater (Supplementary Note 5, Supplementary Figs. 25–29 and Supplementary Movie 3).

Mechanism of the device

To determine the mechanism by which SMCD achieve synaptic function, a nanoscale device was fabricated (Supplementary Fig. 17a). PFSA-PVA and Ag-NWs were coated onto an ITO bottom electrode. A conductive AFM (C-AFM) test was performed by applying a voltage by using a top electrode that had a platinum/iridium (Pt/Ir) tip. The corresponding 2D local current image and current distributions of selected lines were obtained in sample-bias mode (Supplementary Fig. 17b, c). Unlike the conductive filaments that had been observed in previous memristor type work[37–39], under the bias of − 2 V, the current distribution of PFSA-PVA is nearly uniform in all directions. PFSA membrane consists of crystalline regions with long chains of -[CF_2-CF_2]- in any direction and -SO_3 ion clusters forming nanochannels along with the thickness(Fig. 5a), so we suspect that when the voltage spikes are applied, a double electric layer (EDL) will form, rather than a conductive filament. Multiphysics simulation analysis results (Fig. 5b) also show that an EDL is formed on a small scale in the membrane under the point-like Au electrode. However, when applied to the Ag electrode, the voltage rapidly diffuses and becomes uniformly distributed throughout the membrane[32].

To prove the existence of an EDL, we performed electrochemical impedance spectroscopy (EIS) on 5 mm × 5 mm squares of SMCD. The EIS exhibits a typical Nyquist pattern, with the low-frequency region being ray-like (Fig. 5c) and the high-frequency region being 1/4 round. The circular part confirms the existence of EDL[40]. The high-frequency intercept on the real axis ReZ ‘can be used to calculate the ionic resistance[41]. The circular parts of the Nyquist patterns differ. Compared to that of the SMCD composed of pure PFSA, the circular part of the pattern of the SMCD of PFSA modified by PVA shifted to the left and to a higher frequency range. This result indicates that the introduction of PVA increased the ionic conductivity of the SMCD. This change is closely related to the size and number of ion clusters that form in the PFSA membrane.

Two-dimensional Grazing Incidence Wide Angle X-ray Scattering (GIWAXS) test results (Fig. 5d–f) after q-space transformation showed that compared with the original PFSA (Fig. 5e), the bright ring at $q = 10.5\ nm^{-1}$ was more obvious after PFSA was modified by adding PVA (Fig. 5f). This change indicates addition of PVA increases the microcrystalline ratio of (-CF_2-CF_2-) in TFE, increases the randomness of the microcrystalline region, to eliminate obvious anisotropy, tightens the (-CF_2-CF_2-) microhelical main chain(Supplementary Fig. 18), and thus promotes the separation of hydrophilic and hydrophobic phases[42]. Transmission electron microscopy (TEM) was used to visualise the microstructures of PFSA and PFSA-PVA membranes. TEM images show black spots, which are migration channels for hydrated cations[43]. The size and distribution density of these channels (Fig. 5g, h) are more densely distributed with smaller diameters (2.1 nm) in the PFSA-PVA membrane than in the pure PFSA membrane (3.3 nm). After grayscale processing, we quantified the ratio of the nanopore area to the total cross-sectional area and highlighted all nanochannels in red (Supplementary Fig. 18). It was found that the area ratio of nanopores after PVA modification (8.89%) was higher than that of pure PFSA (3.16%). This result indicates that although the diameter (D_i) of individual pores decreased, the total equivalent pore diameter ($\sum D_i$) increased due to the increase in the number of nanochannels and the reduction in the distance between adjacent nanochannels.

The transport of sodium ions is based on the vehicular mechanism (Supplementary Fig. 19), where sodium ions form hydrated sodium ions and then move through nanochannels lined with negatively charged sulfonic acid groups[24,44]. The modification with PVA increases the number of pathways for hydrated sodium ions, enhancing the quantity of sodium ions that can be transported simultaneously and improving the transport efficiency. These results facilitate the migration of more hydrated cations through the nanochannels to the cathode and their capture by Ag-NWs (Fig. 5i); these changes contribute to the enhancement of the synaptic performance of SMCD, resulting in larger current and a higher spike saturation capacity (Supplementary Fig. 20). The PVA modified device maintained continuous current growth for over 500 spikes, notably high among two-terminal synaptic devices (Supplementary Table 2).

Environmental humidity could affect the performance of SMCD by influencing the water content and cation hydration in membranes. Lower humidity environments cause substantial water loss in the SMCD, weakening the dissociation and hydration of cations with water molecules, reducing the number of mobile hydrated cations, and decreasing membrane conductivity[45,46], thereby leading to reduced device current (Supplementary Fig. 21a, b). The encapsulation with polyurethane acrylate (Supplementary Fig. 21d) can improve the environmental stability of SMCD. The long alkyl chains and fluorinated groups form a low-surface-energy layer at the surface, which increases the water contact angle of the encapsulated device to 98.32° (Supplementary Fig. 21e, f). The response current of the encapsulated device remains stable in seven humidity environments (Supplementary Fig. 21b, c). In terms of actuation, SMCD exhibits similar behaviour under different humidity environments. Higher environmental humidity in the unencapsulated device ensures a greater number of hydrated cations within the membrane and their subsequent swelling effect on the cathode side, resulting in higher displacement output (Supplementary Fig. 22a). The maximum displacement at 95% humidity is 9.02 mm, approximately 40 times that at 15% humidity. In contrast, the displacement output of the encapsulated device remains stable at around 10.2 mm in all the above environments. The presence of the encapsulation layer also reduces the oxidation of the Ag component in the device. XRD results (Supplementary Fig. 23) demonstrate that even after 14 days of oxidation, the encapsulated devices remained phase-stable with no obvious peak of Ag_2O. The cyclic stability test curve of the SMCD showed that the performance remained stable throughout the process, without significant changes. Although some attenuation was observed, it remained within an acceptable range. Even after more than 600 cycles, the SMCD retained ~ 80% of its performance (Supplementary Fig. 24)

Discussion

We have presented a synapse-motor coupler device (SMCD), which is a new type of electronic device in which the basic units perform neuromorphic computation, whereas an ensemble of basic units works as an artificial muscle that responds to neuromuscular actuation. The synapse-muscle coupler device can mimic a natural muscle that is innervated by arbitrarily-distributed neuromuscular junctions. These properties originate from special nanoscale ion-transport channels that form in PVA-modified PFSA membrane. An Ag-nanowire forest at one end of these nanoporous structures captured ions, and thus enabled a series of important neuroplasticity behaviours. A functional electronic system that uses this device successfully emulates the threshold, relaxation, and sensitisation of nociceptors. As a proof-of-concept, it successfully replicated the closing movement of the Venus flytrap and achieved multidimensional motion combinations of arbitrary shapes and hazard detection-avoidance robot. SMCD possesses integrated functions of artificial synapses and effectors, providing a unique and simplified strategy for the development of the next generation of neuromorphic viable electronic devices and soft robots, with illustrative examples including soft-bodied bionic hands, crawling agents for pipelines, and similar applications, humanoid neural reflex arcs, and neural prostheses.

https://doi.org/10.1038/s41467-024-55670-4

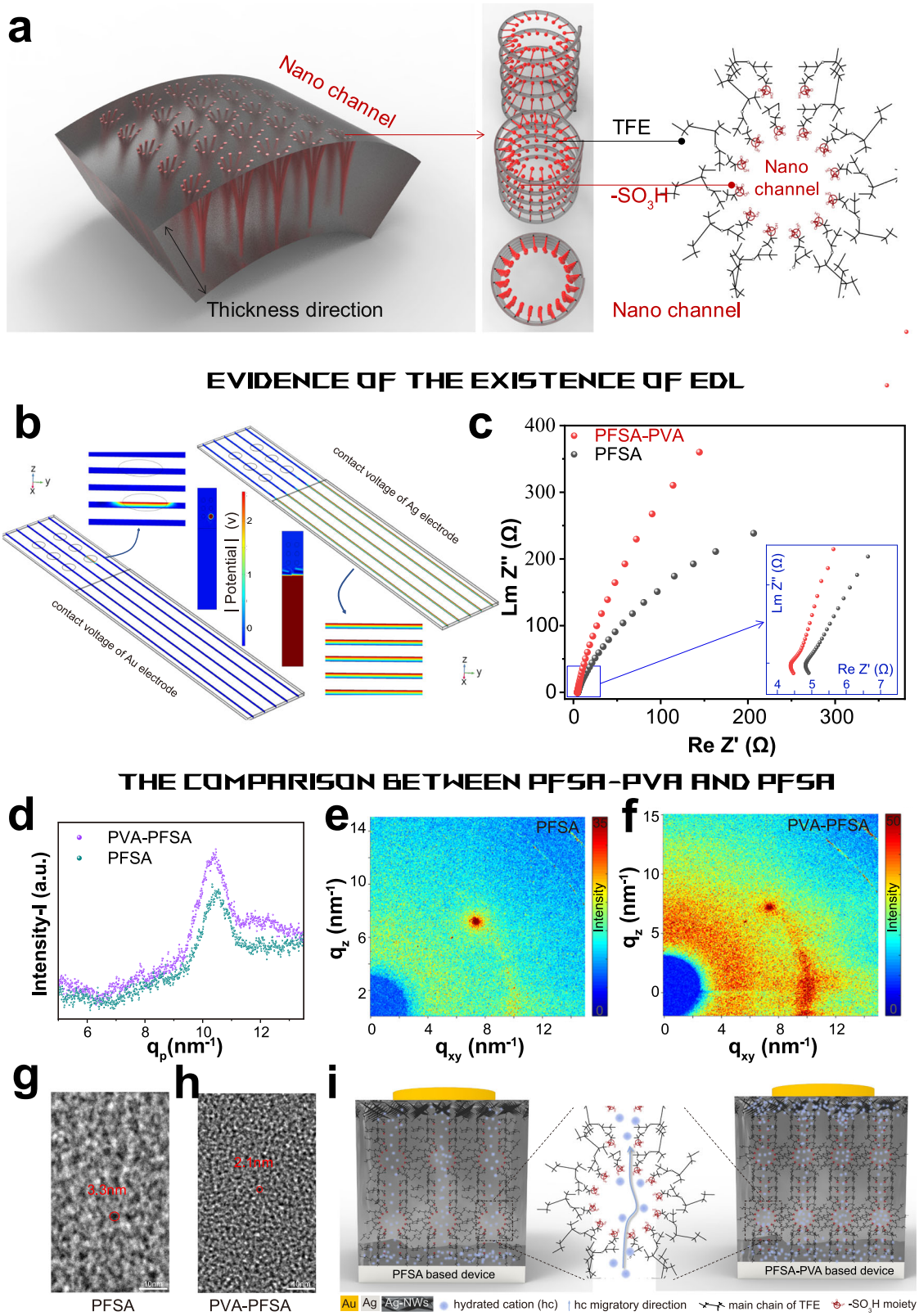

Fig. 5 | The substance transport mechanism and the influence of components in SMCD. a Schematic enlargement of the chemical structure of the nanochannel. **b** Simulation results of electric potential distribution after applying voltages to different functional electrodes. **c** Electrochemical impedance spectroscopy of PVA-PFSA and pure PFSA (inset: enlarged view of the high-frequency region). **d**–**f** Grazing Incidence Wide Angle X-ray Scattering test results of pure PFSA membrane and PVA-PFSA membrane. **g**, **h** TEM image of pure PFSA membrane and PVA-PFSA membrane. **i** Schematic diagram illustrating the comparison of ion channels and ion migration within the membrane before and after PVA modification.

Methods

Preparation of Ag-NWs forest

Ag-NWs forest was prepared by electrochemical deposition. Porous anodic aluminium oxide with an 80 nm aperture is steam-plated with 500 nm Au on one side. The entire gilded surface was encapsulated with hexane oxide to avoid contact with the electroplating solution so that electrodeposition occurred only in the pores.

The encapsulated anodic aluminium oxide was used as the working electrode, Pt slice was used as the auxiliary electrode, and Pt wire was used as the opposite electrode. Electrochemical deposition was performed using cyclic voltammetry in 1 mol/L $AgNO_3$ solution. The voltage range was set from 0 to 0.9 V, and then 600 cycles of scanning were performed at a scan rate of 0.02 V/s. After scanning, the epoxy hexane was washed with dichloromethane. The Ag-NW forest was prepared by etching the anodic aluminium oxide template in a 3 mol/L NaOH solution.

Preparation of composites functional membrane

PVA (Sigma-Aldrich) was dissolved in DI at 80 °C, then stirred for 12 h to obtain the aqueous solution of PVA (5 wt %). Then it was mixed with DMF solvent (Sigma-Aldrich) and 5 wt % Nafion solution (520Cs, DuPont) at a volume ratio of 1:2:20 and stirred for 1 h at room temperature to obtain the casting solution. The solution was mixed by ultrasonication for 30 min of ultrasonic treatment, then poured into a square mould that had an Ag-NW forest at the bottom. The filled mould was moved into a vacuum drying oven for heat curing and stress-relief annealing at three successive temperatures (Supplementary Fig. 5b). The cast membrane was removed from the mould by immersing it in 2 mol/L HCl solution and bringing it to a boil. Subsequent cooling yielded the PFSA-PVA membrane with Ag-NW forest as a composite functional layer.

Characterisations

All electrical measurements were performed using a Keithley 4200 A semiconductor parameter analyser and Keithley 2400 at room temperature. AC impedance was measured using an electrochemical workstation (CHI760, Chenhua, Shanghai). The mechanical information testing is provided by a high-precision force gauge (MARK-10), and the displacement information is obtained through a laser range-finder (Panasonic). The high-precision 3D printing was performed by nanoArch S130 (BMF Material Technology Inc.). AFM images were obtained using a Bruker dimension icon microscope in tapping mode. 1W1A station, Beijing Synchrotron Radiation Facility for provided synchrotron radiation, and the Shiyanjia Lab (www.shiyanjia.com) performed TEM (JEOL JEM 2100 F) characterisation.

Reporting summary

Further information on research design is available in the Nature Portfolio Reporting Summary linked to this article.

Data availability

Source data are provided as a Source Data file. Source data are provided in this paper.

References

1. Wang, Q., Lu, Z., Wang, D. & Wang, K. Mechanosensor for proprioception inspired by ultrasensitive trigger hairs of Venus flytrap. *Cyborg Bionic Syst.* **4**, 0065 (2024).
2. Yao, D. R., Kim, I., Yin, S. & Gao, W. Multimodal soft robotic actuation and locomotion. *Adv. Mater.* **36**, 2308829 (2024).
3. Wang, W. et al. Neuromorphic sensorimotor loop embodied by monolithically integrated, low-voltage, soft e-skin. *Science* **380**, 735–742 (2023).
4. Wang, S. et al. An organic electrochemical transistor for multimodal sensing, memory and processing. *Nat. Electron.* **6**, 281–291 (2023).
5. Rang, H. P. Neuromuscular junction. *Nature* **264**, 386–386 (1976).
6. Liu, J. et al. A bioinspired flexible neuromuscular system based thermal-annealing-free perovskite with passivation. *Nat. Commun.* **13**, 7427 (2022).
7. Shim, H. et al. An elastic and reconfigurable synaptic transistor based on a stretchable bilayer semiconductor. *Nat. Electron.* **5**, 660–671 (2022).
8. Zhou, Y. et al. Computational event-driven vision sensors for in-sensor spiking neural networks. *Nat. Electron.* **6**, 870–878 (2023).
9. Liu, Y., Wang, Y., Li, X. & Hu, Z. A thermally crosslinked ion-gel gated artificial synapse. *Chin. Chem. Lett.* **34**, 107842 (2023).
10. Gao, J. et al. Intrinsic polarization coupling in 2D α-In_2Se_3 toward artificial synapse with multimode operations. *SmartMat* **2**, 88–98 (2021).
11. Yang, J.-Q. et al. Neuromorphic engineering: From biological to spike-based hardware nervous systems. *Adv. Mater.* **32**, 2003610 (2020).
12. Gong, J. et al. Lateral artificial synapses on hybrid perovskite platelets with modulated neuroplasticity. *Adv. Funct. Mater.* **30**, 2005413 (2020).
13. Lv, Z. et al. Self-assembling crystalline peptide microrod for neuromorphic function implementation. *Matter* **4**, 1702–1719 (2021).
14. Zou, J. et al. Muscle-fiber array inspired, multiple-mode, pneumatic artificial muscles through planar design and one-step rolling fabrication. *Natl. Sci. Rev.* **8**, nwab048 (2021).
15. Ji, Z., Yang, S., Shi, G. & Wu, T. Artificial tactile system for pressure monitoring in extracorporeal circulation processes. *APL Mater.* **12**, 041110 (2024).
16. Haines, C. S. et al. Artificial muscles from fishing line and sewing thread. *Science* **343**, 868–872 (2014).
17. Mirvakili, S. M. & Hunter, I. W. Multidirectional artificial muscles from Nylon. *Adv. Mater.* **29**, 1604734 (2017).
18. Dradrach, K. et al. Light-driven peristaltic pumping by an actuating splay-bend strip. *Nat. Commun.* **14**, 1877 (2023).
19. Liu, F., Liu, X., Huang, Q. & Arai, T. Recent progress of magnetically actuated DNA micro/nanorobots. *Cyborg Bionic Syst.* 2022
20. Perez-Guagnelli, E., Jones, J. & D. Damian, D. Hyperelastic Membrane Actuators: Analysis of Toroidal and Helical Multifunctional Configurations. *Cyborg Bionic Syst.* https://doi.org/10.34133/2022/9758460 (2022).
21. Kim, D. S. et al. Preparation of ion exchange membranes for fuel cell based on crosslinked poly(vinyl alcohol) with poly(styrene sulfonic acid-co-maleic acid). *J. Membr. Sci.* **281**, 156–162 (2006).
22. Xie, G. & Okada, T. Water transport behavior in Nafion 117 membranes. *J. Electrochem. Soc.* **142**, 3057 (1995).
23. Peng, J. et al. The effect of hydration number on the interfacial transport of sodium ions. *Nature* **557**, 701–705 (2018).
24. Kreuer, K.-D., Rabenau, A. & Weppner, W. Vehicle mechanism, a new model for the interpretation of the conductivity of fast proton conductors. *Angew. Chem. Int. Ed.* **21**, 208–209 (1982).
25. Zhou, F. & Chai, Y. Near-sensor and in-sensor computing. *Nat. Electron.* **3**, 664–671 (2020).
26. Tang, C. M., Shi, Q. Y., Katchman, A. & Lynch, G. Modulation of the time course of fast EPSCs and glutamate channel kinetics by aniracetam. *Science* **254**, 288–290 (1991).
27. Chen, J. & Xu, W. 2D-materials-based optoelectronic synapses for neuromorphic applications. *eScience* **3**, 100178 (2023).
28. Shim, H. et al. Artificial neuromorphic cognitive skins based on distributed biaxially stretchable elastomeric synaptic transistors. *Proc. Natl. Acad. Sci. USA* **119**, e2204852119 (2022).
29. Gold, M. S. & Gebhart, G. F. Nociceptor sensitization in pain pathogenesis. *Nat. Med.* **16**, 1248–1257 (2010).
30. Lu, Q. et al. Bio-inspired flexible artificial synapses for pain perception and nerve injuries. *Npj Flex. Electron.* **4**, 3 (2020).

31. Dubin, A. E. & Patapoutian, A. Nociceptors: the sensors of the pain pathway. *J. Clin. Invest.* **120**, 3760–3772 (2010).
32. Zhang, K., Julius, D. & Cheng, Y. Structural snapshots of TRPV1 reveal mechanism of polymodal functionality. *Cell* **184**, 5138–5150 (2021).
33. Lu, C. et al. High-performance graphdiyne-based electrochemical actuators. *Nat. Commun.* **9**, 752 (2018).
34. Liu, Q. et al. Electronically configurable microscopic metasheet robots. *Nat. Mater.* https://doi.org/10.1038/s41563-024-02007-7 (2024).
35. Chen, T. et al. Scale-inspired programmable robotic structures with concurrent shape morphing and stiffness variation. *Sci. Rob.* **9**, eadl0307 (2024).
36. Wang, W. et al. Cilia metasurfaces for electronically programmable microfluidic manipulation. *Nature* **605**, 681–686 (2022).
37. Zhang, B. et al. 90% yield production of polymer nano-memristor for in-memory computing. *Nat. Commun.* **12**, 1984 (2021).
38. Wang, Y. et al. Memristor-based biomimetic compound eye for real-time collision detection. *Nat. Commun.* **12**, 5979 (2021).
39. Liu, S. et al. An ultrasmall organic synapse for neuromorphic computing. *Nat. Commun.* **14**, 7655 (2023).
40. Zhang, C. et al. Bioinspired artificial sensory nerve based on Nafion memristor. *Adv. Funct. Mater.* **29**, 1808783 (2019).
41. He, X. et al. Insights into the ionic conduction mechanism of quasi-solid polymer electrolytes through multispectral characterization. *Angew. Chem. Int. Ed.* **60**, 22672–22677 (2021).
42. Kusoglu, A. et al. Impact of substrate and processing on confinement of Nafion thin films. *Adv. Funct. Mater.* **24**, 4763–4774 (2014).
43. Li, Y. et al. Self-healing proton-exchange membranes composed of Nafion–Poly(vinyl alcohol) complexes for durable direct methanol fuel cells. *Adv. Mater.* **30**, 1707146 (2018).
44. Kusoglu, A. & Weber, A. Z. New insights into perfluorinated sulfonic-acid ionomers. *Chem. Rev.* **117**, 987–1104 (2017).
45. Bose, S. et al. Polymer membranes for high temperature proton exchange membrane fuel cell: Recent advances and challenges. *Prog. Polym. Sci.* **36**, 813–843 (2011).
46. Zhang, W. et al. Proton-conductive channels engineering of perfluorosulfonic acid membrane via in situ acid–base pair of metal organic framework for fuel cells. *Adv. Compos. Hybrid. Mater.* **6**, 60 (2023).

Acknowledgements

The authors are grateful for financial support from the National Science Fund for Distinguished Young Scholars of China (T2125005) (W.X.), the National Natural Science Foundation of China (623B2055) (L.J.), the National Key R&D Programme of China under grant NO. 2022YFE0198200, 2022YFA1204500, and 2022YFA1204504 (W.X.), the Shenzhen Science and Technology Project (JCYJ20210324121002008) (W.X.). the Natural Science Foundation of Tianjin (22JCYBJC01290, 23JCQNJC01440) (W.X.), the Key Project of Natural Science Foundation of Tianjin (22JCZDJC00120) (W.X.), the Fundamental Research Funds for the Central Universities, Nankai University (BEG124901, BEG124401) (W.X.), and the National Natural Science Foundation of China (62201290) (C.J.). The authors thank Dr. Bo Liang from Harbin University of Science and Technology and Dr.Tao Yang from Nankai University for helpful discussion.

Author contributions

W.X. and C.Y. initiated the research. J.L., W.X. and C.Y. designed the experiments. J.L. performed the experiments and collected the data. W.X. and J.L. analysed the data and designed the manuscript. W.X. and C.Y. supervised the research. C.J., Q.Y. and Y.N. helped improve data visualisation. All authors discussed the results and commented on the manuscript.

Competing interests

The authors declare no competing interests.

Additional information

Supplementary information The online version contains supplementary material available at https://doi.org/10.1038/s41467-024-55670-4.

Correspondence and requests for materials should be addressed to Cunjiang Yu or Wentao Xu.

Peer review information *Nature Communications* thanks Xiaodong Chen, Il-Kwon Oh, Li Zhang, and the other anonymous reviewer(s) for their contribution to the peer review of this work. A peer review file is available.